Nanoscale

ROYAL SOCIETY OF CHEMISTRY

PAPER

View Article Online
View Journal | View Issue



Cite this: *Nanoscale*, 2025, **17**, 7193

# Bright yellow fluorescent N-doped $Ti_3C_2$ MXene quantum dots as an "on/off/on" nanoprobe for selective $As^{3+}$ ion detection†

Santanu Bera and Susanta Kumar Bhunia *

$Ti_3C_2$ MXene quantum dots (MQDs) are considered to be an emerging nanomaterial in recent times, but the majority of MQDs exhibit limited emission properties in the blue-light region. Longer-wavelength emissive quantum dots are highly desirable in terms of various biological aspects including deep tissue penetration, superior signal-to-noise ratio, reduced radiation damage, *etc*. In this study, bright yellow fluorescent nitrogen-doped MQDs (N-MQDs) were successfully prepared using a one-pot hydrothermal method. The synthesized N-MQDs showed maximum emission at 570 nm upon excitation at a wavelength of 420 nm, with an optimum fluorescence quantum yield of 13.8%. Interestingly, the emission of the N-MQDs was significantly quenched upon the addition of $As^{3+}$ ions. A mechanistic investigation revealed that static quenching was involved in the decrease in the fluorescence *via* the formation of a non-fluorescent complex due to the interaction of the functional groups of the N-MQDs and $As^{3+}$. The quenched fluorescence was surprisingly recovered upon treatment of the complex with 2-amino-6-methoxybenzothiazole (MBTZ). The strong interaction of MBTZ with $As^{3+}$ led to the detachment of the quencher from the N-MQDs, resulting in fluorescence recovery. The re-appearance of the functional groups of the N-MQDs after the addition of MBTZ was confirmed *via* spectroscopic study. Thus, the fluorescence "on/off/on" phenomenon of the N-MQDs nanoprobe was utilised for the instantaneous detection of $As^{3+}$ and MBTZ. The limit of detection values were calculated to be 30 nM and 0.44 μM with a good linearity for $As^{3+}$ and MBTZ, respectively. In addition, a solid sensor has been fabricated to recognize $As^{3+}$ in wastewater, revealing its potential for on-site application in the near future.

Received 8th October 2024,
Accepted 5th February 2025

DOI: 10.1039/d4nr04139a

rsc.li/nanoscale



## 1. Introduction

The consumption of heavy metal ions is increasing due to numerous human activities and rapid industrialisation. A large quantity of these ions spread into the groundwater, which poses a serious threat to all living beings.[1–4] Their intake might have disastrous effects due to their high toxicity and low metabolic activity.[5,6] Arsenic is one of the most hazardous heavy metals, representing a serious worldwide risk to human health and ecosystems.[7,8] Two different forms of arsenic exist in aqueous environments, namely, arsenite ($As^{3+}$ form) and arsenate ($As^{5+}$ form).[9,10] However, the $As^{3+}$ ion is more hazardous and stable than the $As^{5+}$ ion. According to the World Health Organization (WHO), the maximum allowed level of arsenic in drinking water is 10 parts per billion (ppb).[11] Ingestion of $As^{3+}$ leads to variety of health concerns such as lung cancer, skin diseases, liver cancer, cardiovascular problems, and respiratory disorders.[12–14] Therefore, suitable monitoring of $As^{3+}$ ions in drinking water and other environmental sources with greater efficacy in terms of selectivity and sensitivity need to be adopted. Several techniques are used for the detection of $As^{3+}$ ions such as ion chromatography, coupled plasma mass spectrometry, atomic absorption spectroscopy (AAS) and high-performance liquid chromatography (HPLC).[15–18] The above-mentioned techniques are expensive and require skilled personnel for sample preparation. In contrast, fluorometric analysis is very well known due to its simple, fast, cost-effective, and in-field/real time monitoring.[19–24]

MXenes are an emerging class of layered 2D nanomaterials.[25] They have numerous distinct properties, such as high surface area, high conductivity, and physical and chemical stability. These exceptional properties of MXene make it highly interesting for various applications.[26–29] MXene can be obtained by chemical etching of "A" in a MAX phase with the general formula of ($M_{n+1}AX_n$), where M denotes the d-transition metals (like Ti, Nb, Ta, Mo etc.), "A" represents the main group (III or IV) elements of the periodic table (such as Al, Ga etc.) and X is nitride or carbide.[30,31] They have several forms, but the most common one is $Ti_3C_2$. $Ti_3C_2$-derived MQDs with

*Department of Chemistry, School of Advanced Sciences, Vellore Institute of Technology, Vellore 632014, India. E-mail: susanta.bhunia@vit.ac.in, susanta.chem@gmail.com*

† Electronic supplementary information (ESI) available. See DOI: https://doi.org/10.1039/d4nr04139a

a zero-dimensional structure possesses superior properties in terms of photoluminescence and quantum yields.[32,33] According to previous findings, MQDs show photoluminescence due to quantum confinement and edge effects. These excellent properties make it an excellent choice for various applications such as immunomodulation, energy storage, biosensing, photoelectrical devices, environmental remediation and heavy metal detection.[34–36] These quantum dots show tremendous efficiency towards the detection of ions and organic pollutants (such as $Cu^{2+}$, $Fe^{3+}$, $Co^{2+}$, $Ag^{+}$, Alizarin red and histidine) *via* modulation of their fluorescence properties.[28,37–40] To the best of our knowledge, there have been no reports of the fluorometric detection of $As^{3+}$ ions using MQDs.

Herein, for the first time we report the synthesis of bright yellow fluorescent nitrogen-doped MQDs (N-MQDs) with a maximum fluorescence quantum yield of 13.8% and have selectively detected $As^{3+}$ ions. The N-MQDs were prepared *via* a one-pot hydrothermal method from MXene as the MQD source and *o*-phenylenediamine as the nitrogen source. The fluorescence intensity of the N-MQDs experienced a quenching of 93% after treatment with $As^{3+}$ ions. Interaction of the functional groups on the surface of the N-MQDs with $As^{3+}$ and static quenching were proposed to explain the emission quenching. The quenched fluorescence in the N-MQDs + $As^{3+}$ complex was reversed after the addition of MBTZ. The strong affinity of the nitrogen and sulphur atoms in MBTZ with $As^{3+}$ results in the detachment of $As^{3+}$ from the surface of the N-MQDs and recovery of their fluorescence. The synthesized N-MQDs were adsorbed on Whatman filter paper and cigarette filters for solid sensor application. The fabricated sensors displayed unique identification toward $As^{3+}$ in wastewater without any leaching of the N-MQDs. Furthermore, the N-MQDs were successfully applied as a fluorescent ink. This type of nanoprobe will offer the identification of toxic pollutants towards wastewater treatment in the near future.

## 2. Experimental section

### 2.1. Chemicals

Titanium aluminium carbide ($Ti_3AlC_2$, 99%) was purchased from NANOSHEL Ltd (UK). Arsenic(III) iodide (99%) was bought from Sigma-Aldrich. *o*-Phenylenediamine (*o*-PD) (99%) and sodium arsenate dibasic heptahydrate were purchased from SD Fine Chem Ltd. Manganese(II) chloride (99%), chromium(III) sulfate (99%), and sodium chloride (NaCl) (99%), were purchased from SRL Pvt. Ltd. Lead(II) chloride (98%) was obtained from LOBA Chemicals Pvt. Ltd. Hydrofluoric acid (49%), 2-amino-6-methoxybenzothiazole (MBTZ) (98%), mercury(II) acetate (98%), and cadmium(II) chloride (98%) were purchased from Avra Synthesis Pvt. Ltd. *N*,*N*-Dimethylformamide (DMF) was bought from Spectrochem Pvt. Ltd. All the aforementioned chemical reagents were used without additional purification.

### 2.2. Instrumentation

A 200 kV JEOL JEM-2100F microscope was used to capture high-resolution transmission electron microscopy (HRTEM) images of the N-MQDs. The structural morphologies of MAX and MXene were studied *via* scanning electron microscopy (SEM) and field emission scanning electron microscopy (FESEM) using EVO 18 Carl Zeiss and Thermo Fisher FEI QUANTA 250 FEG, respectively. A JASCO V-730 spectrophotometer was used for measurement of the UV-vis absorption spectra of the N-MQDs solution. A Synergy H1–H1M multimode fluorescence spectrophotometer was used to measure the excitation and emission spectra of the N-MQDs. X-ray photoelectron spectroscopy (XPS) and Fourier transform infrared spectroscopy (FT-IR) of the N-MQDs were carried out *via* a K ALPHA – M/s Thermo Fisher Scientific instruments (UK) and a SHIMADZU IRAffinity-1 spectrophotometer. Fluorescence lifetime of N-MQDs was measured using HORIBA Scientific Delta Pro-DD lifetime system *via* Time-Correlated Single Photon Counting (TCSPC) mode. X-ray diffraction (XRD) of MAX, MXene and N-MQDs was conducted using a D2 PHASER desktop/max-RAX-ray diffractometer (Bruker, Germany) from 10° to 90° with Cu Kα radiation, a 30 kV accelerating voltage, and a 10 mA current. Hydrodynamic diameter and zeta potential were measured using a Horiba Scientific SZ 100 instrument.

### 2.3. Synthesis of $Ti_3C_2$ (MXene)

Firstly, 1 g $Ti_3AlC_2$ powder was added slowly to 10 mL 49% hydrofluoric acid (HF) solution and the mixture was continuously stirred for 48 h. The resulting black-colored solution was centrifuged at 4000 rpm for 60 min, followed by washing with deionized water several times to obtain neutral pH of the supernatant. Next, the precipitate was collected and dried overnight in a hot air oven to obtain MXene.

### 2.4. Synthesis of N-MQDs

N-MQDs were prepared from MXene nanosheets *via* a hydrothermal method. In brief, 5 mg MXene powder was dispersed in 5 mL deionized water and sonicated for 1.4 h. Next, 2.5 mg *o*-PD was added to the solution, and the mixture was hydrothermally heated at 150 °C for 14 h. The resultant bright yellow fluorescent N-MQDs were purified using a 0.22 μm syringe filter. The filtrate was again purified *via* a dialysis membrane. The purified dialyzed solution was used for the various characterizations and applications.

### 2.5. Detection of $As^{3+}$ ions

The synthesized N-MQDs were designed to selectively recognise $As^{3+}$ ions in water. Aqueous solutions with different concentrations of $As^{3+}$ ions (0.03–0.2 mM) were added to 500 μL of N-MQDs at room temperature followed by instantaneous recording of the fluorescence properties. For other analytes, the aqueous solutions of N-MQDs were incubated with the different metal ions ($Cu^{2+}$, $Pb^{2+}$, $Mn^{2+}$, $Na^{+}$, $Cd^{2+}$, $Cr^{3+}$ and $As^{5+}$) at a maximum concentration of 0.2 mM. Fluorescence

 

spectra were measured at an excitation wavelength of 420 nm, and emission intensity was collected at 570 nm.

### 2.6. Detection of MBTZ

MBTZ solutions of different concentrations (0.39–5.66 mM) were incubated with an N-MQDs–$As^{3+}$ mixture containing 0.2 mM $As^{3+}$. Fluorescence spectra were measured under an excitation wavelength of 420 nm to record the emission response.

## 3. Results and discussion

### 3.1. Synthesis strategy of N-MQDs

Bright yellow emissive N-MQDs were synthesized *via* a simple hydrothermal method from a mixture of MXene and *o*-PD. The MXene nanosheets were first prepared *via* an etching process. Hydrofluoric acid was used as the etching agent, which removes aluminium from the stacked MAX phase, resulting in layered MXene nanosheets. This is quite similar to the synthesis of graphene *via* graphite exfoliation. After hydrothermal treatment of the MXene and *o*-PD mixture, the black-colored solution became dark brown, indicating the emergence of the N-MQDs. The solution was purified to remove unreacted molecules and some of the bulk sheets. The purified N-MQDs solution displayed very bright yellow emission under 365 nm UV lamp irradiation. The synthetic procedure for the N-MQDs and recognition of $As^{3+}$ and MBTZ *via* the fluorescence "on–off–on" strategy are represented in Scheme 1.

### 3.2 Characterization of N-MQDs

The structural and optical properties of the N-MQDs were studied using various microscopic and spectroscopic techniques. SEM and FESEM images of MAX phase and MXene nanosheets are presented in Fig. 1A and B. They indicate that the delaminated MXene nanosheets were formed from bulk smooth-structured $Ti_3AlC_2$ *via* the etching process using HF.[40] The removal of aluminium from the MAX phase was confirmed from the EDX spectrum in Fig. S1, ESI,† which shows the existence of titanium, carbon, and a small amount of fluorine. The elemental mapping of these elements is also shown in the figure. A top-down approach was employed to synthesize MQDs from MXene using a hydrothermal method that breaks down the sheet structure into nanoparticles.[28] The TEM and HRTEM images in Fig. 1C reveal the formation of small-sized zero-dimensional N-MQDs. The interplanar spacing of the N-MQDs was measured to be 0.24 nm, indicating crystalline nature and the absence of damage to the internal structure of the N-MQDs (inset image).[41] The average diameter of the synthesized N-MQDs was extracted from the TEM image; the nanoparticles are evenly distributed between 1.5–6.5 nm with an average diameter of 3.3 nm (Fig. 1D).

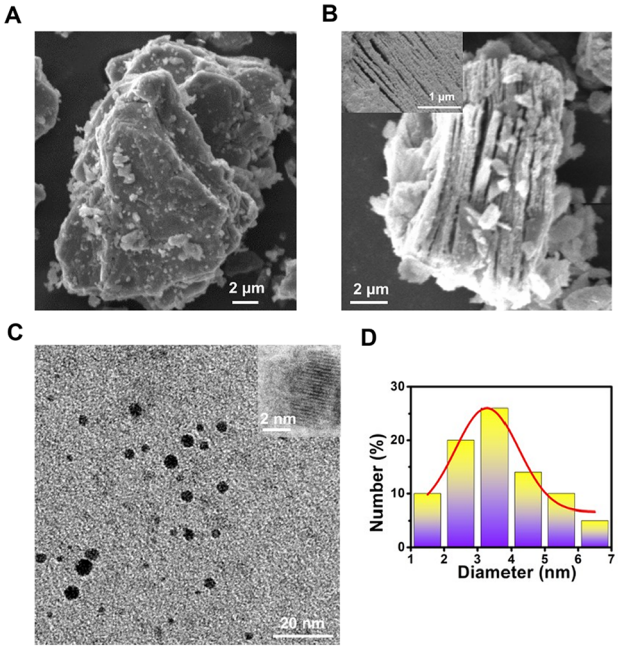


**Fig. 1** SEM images of the (A) MAX phase and (B) MXene nanosheets. Inset is an FESEM image of the MXene nanosheets. (C) TEM image of N-MQDs. Inset is an HRTEM image. (D) Size profile of the N-MQDs.

The optical properties of the N-MQDs were measured *via* absorbance- and fluorescence-based measurements. The UV-vis absorbance spectrum is shown in Fig. 2A and exhibits two strong peaks. The peaks appearing at 258 nm and 420 nm

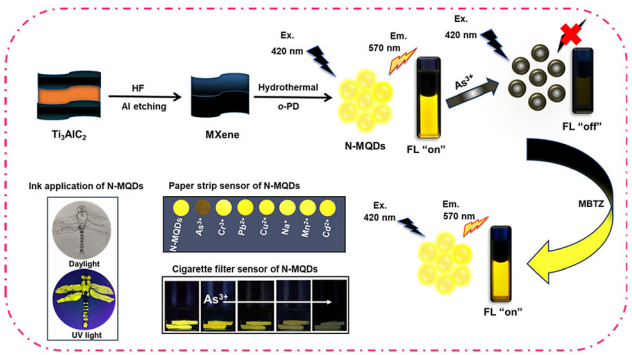


**Scheme 1** Schematic presentation of the synthesis of yellow fluorescent N-MQDs and recognition of $As^{3+}$ and MBTZ.

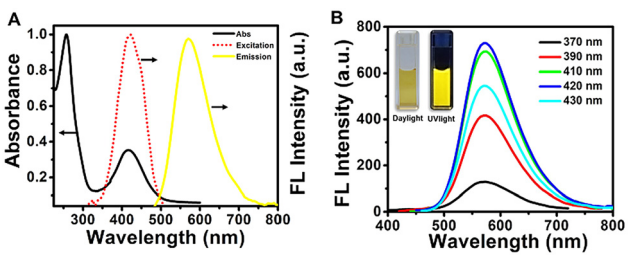


**Fig. 2** (A) UV-vis absorbance, fluorescence excitation and emission spectra of N-MQDs. (B) Emission spectra of N-MQDs at different excitation wavelengths. Daylight and fluorescence digital images of N-MQDs (inset).

correspond to π–π* and n–π* transitions, respectively.[39,42,43] The doping of hetero-elements such as nitrogen and oxygen into the N-MQDs matrix led to the latter transition.[40,44] The photoluminescence excitation spectrum showed a strong intense peak at 420 nm. While excited at 420 nm, the maximum emission intensity was observed at 570 nm. These three spectra are shown in Fig. 2A. Next, the emission spectra of the N-MQDs were measured at different excitation wavelengths between 370 and 430 nm. It can be noted in Fig. 2B that the maximum emission wavelength did not shift, indicating a narrow distribution of the surface energy states due to surface-passivated hetero-atoms.[43] An aqueous dispersion of N-MQDs was placed in a quartz cuvette, and images were captured under daylight and a UV lamp. Very bright fluorescence was observed from the N-MQDs, as shown in the inset of Fig. 2B. The fluorescence quantum yield was measured against fluorescein as a reference, and the maximum value was found to be 13.8%. A table (Table 1) is presented for the comparison of our synthesized N-MQDs with previous reports. It is clear that most of the previous reports involve blue- and green-emissive MQDs. Our synthesized N-MQDs show yellow emission with a high fluorescence quantum yield so far. Longer-wavelength emissive (yellow or red) quantum dots are highly desirable in biological applications. The origin of such high brightness with yellow fluorescence is due to the doping of sufficient hetero-atoms and surface passivation in the N-MQDs.[20] Hetero-atoms induce more defect sites in the matrix of the MQDs, which imparts longer wavelength emission and bright fluorescence. This was confirmed by performing some experiments. Blue fluorescent MQDs with very low brightness were formed when the MXene nanosheets alone were hydrothermally treated under the same conditions (Fig. S2, ESI†). Furthermore, when the MXene nanosheets were heated with a benzene derivative with a smaller number of nitrogen-containing functional groups (such as aniline), the resultant solution also showed blue fluorescence with very low fluorescence. From these experiments, it can be concluded that a sufficient amount of hetero-atoms is required for fluorescence tuning.

The atomic combination and occupancy of functional groups on the surface of the N-MQDs was analysed *via* an XPS study. The presence of four major peaks was observed in the survey spectrum, as shown in Fig. S3, ESI.† The peaks at 284.3 eV, 399.4 eV, 458.2 eV, and 532.6 eV were ascribed to C 1s, N 1s, Ti 2p, and O 1s, respectively. High-resolution spectra of the elemental XPS peaks were obtained to examine the specific functional groups. The Ti 2p XPS spectrum showed two deconvoluted peaks with binding energies at 458.2 eV and 463.7 eV, representing Ti–O and Ti–C bonds, respectively (Fig. 3A). This indicates that the hydrothermal reaction assists in forming Ti–O bonds from Ti–C bonds on the surface and edges of N-MQDs.[37,46]

Two deconvoluted peaks at 284.5 eV and 286.7 eV were observed in the case of C 1s, as displayed in Fig. 3B.[40,46] These peaks correspond to C–C and C–O/C–N groups, respectively. The two peaks of N 1s at 398.8 eV and 400.6 eV indicate the presence of C–N and/C═N and N–O groups, respectively (Fig. 3C).[47] The presence of the groups Ti–O and Ti-OH/C═O was confirmed from the two respective deconvoluted peaks at 529.5 eV and 531.7 eV in the case of O 1s (Fig. 3D).[48] Thus, the results confirm that nitrogen-containing and oxygen-containing functional groups were present in the N-MQDs and that the MXene structure was still maintained. The Fourier transform infrared (FT-IR) spectrum also revealed the presence of various functional groups on the surface of the MXene and N-MQDs, as shown in Fig. 4A. The broad peak centred at 3386 $cm^{-1}$ was attributed to –NH and –OH bonds in the N-MQDs.[49] The peak at 1630 $cm^{-1}$ represents the stretching vibration of the C═O bond.[44] The peak appearing at 1375 $cm^{-1}$ corresponds to the C–N stretching vibration. Thus, the results further confirm the successful doping of nitrogen

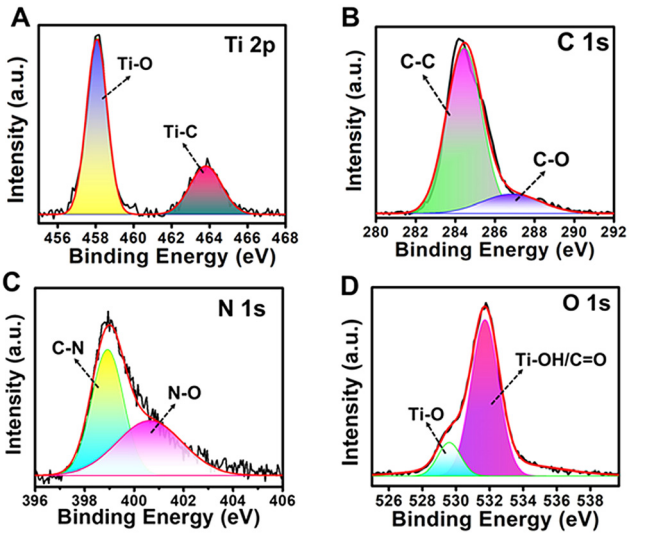


**Fig. 3** High-resolution XPS spectra of (A) Ti 2p, (B) C 1s, (C) N 1s, and (D) O 1s in the N-MQDs.

**Table 1** Comparison of the synthesis of MQDs

| Precursor(s) | Preparation method | Fluorescence | $\lambda_{max}$ (Em/Ex) nm | Quantum yield (%) | Ref. |
|---|---|---|---|---|---|
| $Ti_3C_2$ powder and 3-aminopropyltriethoxysilane | Solvothermal | Blue | 427/330 | 15.4 | 37 |
| $Ti_3C_2$ powder, KOH and DMF | Solvothermal | Blue | 420/335 | 14.46 | 38 |
| $Ti_3C_2$ powder, $H_3PO_4$ and formamide | Microwave | Green | 500/390 | 21.5 | 45 |
| $Ti_3C_2$ powder, $HNO_3$ and ethylenediamine | Ultrasonication | Blue | 453/365 | 20.35 | 19 |
| $Ti_3C_2$ powder, methanol and *o*-phenylenediamine | Solvothermal | Yellow | 580/420 | 5.42 | 39 |
| $Ti_3C_2$ powder and *o*-phenylenediamine | Hydrothermal | Yellow | 570/420 | 13.8 | This work |

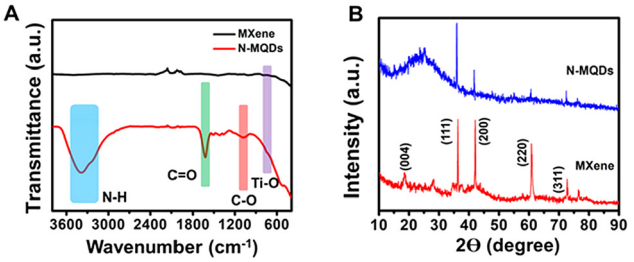


Fig. 4 (A) FT-IR and (B) XRD spectra of MXene and N-MQDs.

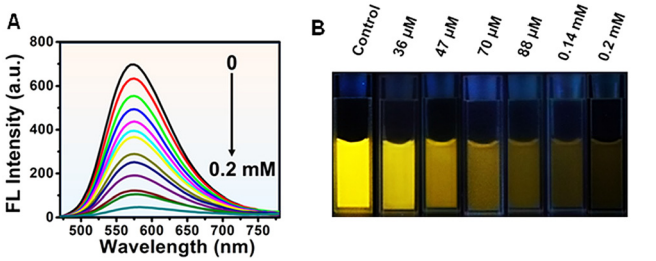


Fig. 5 Response of the fluorescence of the N-MQDs to $As^{3+}$ ions. (A) Emission spectra of N-MQDs in the presence of different concentrations of $As^{3+}$ ranging from 36 μM to 0.2 mM. (B) Fluorescence digital images of the N-MQDs after the addition of the specified doses of $As^{3+}$.

into the N-MQDs. The peak at 1074 $cm^{-1}$ represents the C–O bond. The vibration of the Ti–O bond was recorded at 752 $cm^{-1}$.[46] A broad peak at 560 $cm^{-1}$ corresponds to the Ti–C bond.[38] This reveals that abundant hydroxyl and terminal oxygens were decorated onto the surface of the N-MQDs.

The crystalline nature of the synthesized N-MQDs was analysed using the XRD technique. As shown in Fig. 4B, the diffraction peaks of MXene at 18.4°, 36.2°, 42.8°, 60.8°, and 72.7° were attributed to the corresponding (004), (111), (200), (220) and (311) planes, respectively, confirming the hexagonal crystalline phase.[50] The N-MQDs showed similar peaks to the MXene nanosheets; in addition, an amorphous peak at 24° indicated the crystallinity of the N-MQDs was slightly reduced.[19] Notably, $Ti_3AlC_2$ displayed peaks at 10°, 36.3°, 39.4°, 60.9°, and 74.3° corresponding to the (002), (104), (105), (110), and (118) planes, respectively, as shown in Fig. S4, ESI.† These outcomes support the existence of crystallinity in the N-MQDs, similar to MXene.[50] To examine their photostability, an aqueous dispersion of N-MQDs were exposed to tungsten lamp irradiation (>400 nm wavelength) for 1 h. Aliquots were collected at different times to measure the emission spectra. The fluorescence digital images and emission spectra of the N-MQDs are shown in Fig. S5, ESI.† The results demonstrate an insignificant loss of fluorescence intensity in the N-MQDs and prove their good photostability.

### 3.3. Fluorescence response of the N-MQDs to different ions and selectivity study

To explore their sensing applications, aqueous solutions of the synthesized N-MQDs were incubated with various metal and non-metal ions. The ions $As^{3+}$, $Pb^{2+}$, $Cu^{2+}$, $Na^{+}$, $Mn^{2+}$, $Cd^{2+}$, $Cr^{3+}$ and $As^{5+}$ were used in this study. A specific concentration (0.2 mM) of each analyte was added to separate N-MQDs solutions and the fluorescence was immediately measured. The changes in the maximum fluorescence intensity at 570 nm of N-MQDs in the presence of the analytes have been plotted in Fig. S6, ESI.† The emission intensity was dramatically quenched in case of treatment with $As^{3+}$, and the value was measured to be 93%. Slight quenching was observed for some of the analytes; however, the changes were insignificant compared to that for $As^{3+}$. Fig. S7, ESI,† presents the digital images of the emission of the N-MQDs with the incubation of the various ions, in which similar results to those in Fig. S6, ESI,† were observed. Next, different concentrations of $As^{3+}$ between 36 μM and 0.2 mM were incubated with the N-MQDs aqueous solution to calculate the limit of detection and binding constant. It can be observed from Fig. 5A that the fluorescence intensity of the N-MQDs was gradually attenuated with increasing $As^{3+}$ concentration, with a maximum reduction of 93% against 0.2 mM of $As^{3+}$. Fluorescence digital images with variation of the $As^{3+}$ concentration were captured under a UV lamp, and the gradual decrease in the emission brightness (Fig. 5B) was in the same order as the result in Fig. 5A.

As the fluorescence response of N-MQDs is $As^{3+}$-dose-dependent, the value of the LOD is easily measurable. It was calculated by plotting the emission intensity changes against the concentration of $As^{3+}$, as shown in Fig. S8, ESI.† It showed a very good linear relationship with a coefficient value of 0.988, and the LOD was measured to be 30 nM. This value is good enough to detect $As^{3+}$ and is comparable with those of other nanoprobes.[51–54] The quenching constant was also measured using the Stern–Volmer equation, and the value was found to be $8.6 \times 10^4$ $M^{-1}$. The high order of magnitude of this value indicates very strong binding of the N-MQDs with $As^{3+}$.[55] Surface-decorated amine and oxygen-containing functional groups interact and tightly bind with positively charged $As^{3+}$.[55,56] This could result in charge transfer between the analyte and fluorophore, followed by the formation of a non-fluorescent complex.

### 3.4. Detection of MBTZ

The synthesized N-MQDs were used as a fluorescent "on–off–on" nanoprobe to detect MBTZ. MBTZ is primarily recognised for its potential health hazards, including skin irritation, serious eye irritation, and respiratory irritation. First, the bright yellow fluorescent N-MQDs were incubated with 0.2 mM $As^{3+}$ to achieve the emission-quenched N-MQDs–$As^{3+}$ complex. Next, MBTZ (concentration of 5.66 mM) was added to the complex. It was observed that quenched fluorescence was restored immediately. To examine the restoration response, different concentrations (0.39–5.66 mM) of MBTZ were added to the quenched complex and the fluorescence spectra were measured instantly. Fig. 6A shows the gradual increase in the fluorescence intensity with increasing concentration of MBTZ. Fluorescence digital images were also captured and clearly

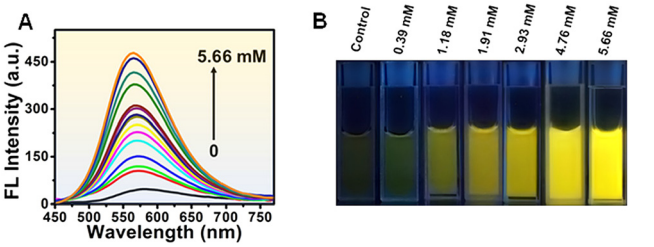


**Fig. 6** (A) Fluorescence response of N-MQDs + $As^{3+}$ after the addition of MBTZ (concentration range 0.39–5.66 mM). (B) Fluorescence digital images of solutions with the indicated MBTZ concentrations.

indicate the gradual enhancement of the brightness with MBTZ concentration (Fig. 6B). The value of the LOD for the MBTZ response was also calculated. A linear response was recorded as shown in Fig. S9, ESI,† and the LOD was measured to be 0.44 μM with a good coefficient.

### 3.5. Mechanism of the fluorescence quenching and recovery of the N-MQDs

Various spectroscopic studies revealed the presence of nitrogen- and oxygen-containing functional groups on the surface of the N-MQDs. After incubation with $As^{3+}$, the electron-rich nitrogen and oxygen groups interact with the positively charged arsenic ions. This might result in charge transfer between the fluorophore and analyte, resulting in the formation of a non-fluorescent complex. The quenching of fluorescence can occur *via* a variety of mechanisms, such as static quenching, dynamic quenching, inner filter effect (IFE), and fluorescence resonance energy transfer (FRET). In the case of static quenching, ground state complex formation will take place and obvious changes in the absorbance properties of the N-MQDs should be observed. In addition, the fluorescence lifetime of the N-MQDs should be unchanged before and after the addition of the analyte, and variation of the temperature would not strongly affect the fluorescence properties. In contrast, collisional deactivation will take place in dynamic quenching. Significant changes in the fluorescence lifetime of the N-MQDs prior to and after the addition of analyte are also a factor responsible for dynamic quenching. In case of IFE and FRET, a notable overlap of absorption spectrum of the $As^{3+}$ with the excitation/emission spectrum of the N-MQDs should be observed. Several experiments were performed to determine the quenching mechanism behind the decrease in the emission of the N-MQDs. The UV-vis absorbance spectrum of the N-MQDs was measured after treatment with different individual metal ions. It can be observed in Fig. 7A that no obvious changes were recorded for metal ions other than $As^{3+}$. In contrast, the absorption intensities corresponding to π–π* and n–π* in the N-MQDs were decreased after incubation with $As^{3+}$. In addition, the peaks were right-shifted to 265 nm and 450 nm. This might be due to the effective interaction of $As^{3+}$ and the functional groups resulting in close proximity of the fluorophores. No changes were observed in the case of other

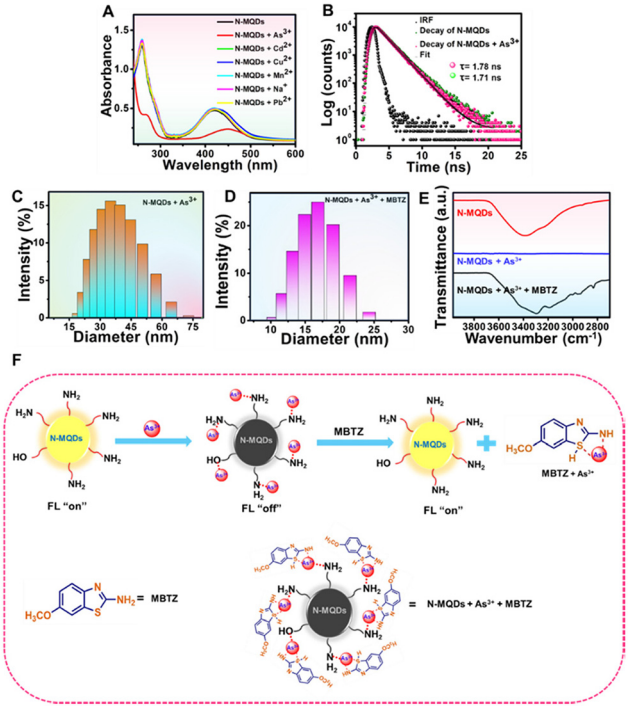


**Fig. 7** (A) UV-vis absorbance spectra of N-MQDs before and after the addition of different analytes, showing a noticeable change for $As^{3+}$. (B) Fluorescence lifetime decay of the N-MQDs with and without treatment with $As^{3+}$. Hydrodynamic diameter of (C) $As^{3+}$-incubated N-MQDs solution and (D) MBTZ-incubated N-MQDs–$As^{3+}$ system. (E) FT-IR spectra of N-MQDs after addition of $As^{3+}$ and MBTZ. (F) Possible "on–off–on" mechanism of the N-MQDs after treatment with $As^{3+}$ and MBTZ.

ions. The fluorescence lifetime of the N-MQDs was measured before and after the addition of $As^{3+}$, and the values were 1.78 ns and 1.71 ns, as shown in Fig. 7B. However, this change is insignificant. The changes in the fluorescence intensity of the quenched complex were also measured at different temperatures in the range of 0–60 °C. As shown in Fig. S10, ESI,† no significant variation of the intensities with varying temperature was observed. The binding constant of the analyte with N-MQDs was calculated using a Stern–Volmer plot and shows a high order of magnitude. All these results confirm the occurrence of static quenching in the fluorescence response of the N-MQDs towards $As^{3+}$.[47,57–59] The hydrodynamic diameter of the N-MQDs was measured before and after $As^{3+}$ treatment to prove the interaction. The average diameter of the N-MQDs was calculated to be 10.34 nm, as shown in Fig. S11, ESI;† $As^{3+}$ treatment increased the diameter to 35.03 nm (Fig. 7C). This indicates that effective interaction between $As^{3+}$ and the functional groups of the fluorophore resulted in an increase in the hydrodynamic diameter of the N-MQDs. Their zeta potential was also measured to check the surface charge and their interaction with analytes. The N-MQDs showed a positive value of +7.5 mV, while $As^{3+}$ treatment enhanced the surface charge to a more highly positive value (+16.2 mV). This indicates effective interaction of $As^{3+}$ with the surface functional groups of the N-MQDs. Next, another target was to recover the

quenched fluorescence of the N-MQDs. Upon the treatment with MBTZ in N-MQDs–$As^{3+}$ solution, the quenched fluorescence was restored. The hydrodynamic size of the MBTZ-incubated N-MQDs–$As^{3+}$ solution was measured, and it showed a value of 16.84 nm (Fig. 7D). This means that MBTZ might have strong affinity to bind with $As^{3+}$, resulting in the N-MQDs becoming free and the fluorescence being restored. In parallel, the high positive surface charge of the N-MQDs + $As^{3+}$ complex was reduced to +9.5 mV after treatment with MBTZ further assisted the detachment of $As^{3+}$ from the N-MQDs surface. To prove this interaction, FTIR analysis was carried out. Fig. 7E displays the disappearance of the broad peak in the range of 3400 to 2800 $cm^{-1}$ of the N-MQDs after $As^{3+}$ incubation. This indicates that the vacant 4p orbital of $As^{3+}$ can easily accept electrons from electron-rich nitrogen- and oxygen-containing functional groups in the N-MQDs.[55] Thus, the functional groups of the N-MQDs became involved in interaction with $As^{3+}$, and their corresponding transmittance peaks disappeared. After treatment of the N-MQDs + $As^{3+}$ complex with MBTZ, these peaks were restored. This suggests that the interacting nitrogen and oxygen functional groups became free and showed their transmittance characteristics. This could be due to the methoxy group ($-OCH_3$) of MBTZ showing a (+)-mesomeric effect, resulting in rich electron density on the benzothiazole ring. The availability of electron density also increases on the sulphur and nitrogen atoms of MBTZ, and can strongly bind with $As^{3+}$.[60,61] In addition, the FTIR spectra of MBTZ and N-MQDs + $As^{3+}$ + MBTZ are presented in Fig. S12, ESI.† The peaks at 1640 $cm^{-1}$ and 710–545 $cm^{-1}$ corresponding to the N–H and C–S stretching vibrations of MBTZ became broadened after incubation with the N-MQDs + $As^{3+}$ mixture. These results confirm that $As^{3+}$ ions bind with the S and N atoms of MBTZ.[47,62] Therefore, it can be concluded that the recovery of the transmittance peaks is due to the detachment of $As^{3+}$ from the N-MQDs surface. A typical representation of fluorescence "on–off–on" strategy is shown in Fig. 7F.

### 3.6. Detection of $As^{3+}$ in the solid phase

To examine the real field applicability of synthesized N-MQDs, paper strip and cigarette filter sensors have been developed. The solid sensor selectivity towards $As^{3+}$ was first tested. Whatman filter paper was cut into small round-shaped pieces and immersed in an aqueous dispersion of N-MQDs, followed by drying at ambient temperature. Next, the paper pieces were dipped in different metal and non-metal ion solutions (concentration of 0.2 mM). Afterwards, fluorescence digital images of the N-MQDs-coated papers were captured after drying. Fig. 8A shows the very prominent fluorescence quenching in the case of $As^{3+}$ incubation. The other ions did not affect the fluorescence of the N-MQDs significantly. This indicates the very high selectivity of the N-MQDs toward $As^{3+}$. To see the response of the N-MQDs to a low concentration of $As^{3+}$, square-shaped N-MQDs-coated paper strips were incubated with different concentrations of $As^{3+}$ aqueous solution. It was observed that the emission brightness of the N-MQDs gradually decreased with increasing $As^{3+}$ and finally became non-fluorescent at a 0.2 mM $As^{3+}$ concentration (Fig. 8B). Cigarette filters were also applied as another solid sensor as they can detect $As^{3+}$ before it reaches the health system. Cigarette filters are one of the most prevalent sources of solid waste litter in the world. Cigarette filters are made of cellulose acetate, which is intended to entirely or partly preserve particulate smoke components including nicotine, tar, polycyclic aromatic hydrocarbons (PAHs) and toxic metals.[63,64] These contaminants can leach out into the environment from cigarette filters and contaminate soil and ground water. These pollutants also have the potential to bioaccumulate and find their way into food chains through biomagnification.[63] Cigarette filters are discarded into the environment after smoking and remain stable for a long time. They have excellent absorption properties. We used this property through simply dipping them in N-MQDs aqueous solution. Next, the filters with adsorbed N-MQDs were immersed in different concentrations of $As^{3+}$ solution. Fig. 8C shows a gradual decrease in fluorescence brightness with $As^{3+}$ concentration similar to that observed in Fig. 8B. The high fluorescence quantum yield of the N-MQDs was utilised in a fluorescent ink application. For this, the N-MQDs were used as ink, and a dragonfly was drawn on plain paper. A fluorescent digital image of the picture was captured after drying, and it showed very bright emission, as shown in Fig. 8D.

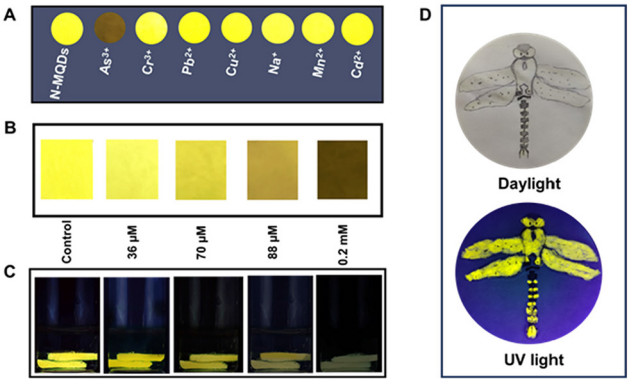


Fig. 8 Solid phase detection of different ions and various concentrations using N-MQDs. (A) Digital images of N-MQDs paper strips under a 365 nm UV lamp after immersion in different ions. (B) Digital images of N-MQDs paper strips with various concentrations of $As^{3+}$ ions (ranging from 36 μM to 0.2 mM). (C) Cigarette filters after treatment with the indicated $As^{3+}$ concentrations. (D) Daylight and fluorescent images of a "dragonfly" drawn using N-MQDs.

### 3.7. Real sample analysis

Analysis was also performed to detect $As^{3+}$ in real water samples. For this, water from different sources, namely, tap, river and seawater, were collected. The water samples were filtered using a 0.22 μm syringe filter to remove large-sized particles. Next, a certain concentration of $As^{3+}$ (0.088 mM) was spiked into the water samples, followed by incubation with the N-MQDs. Afterwards, the fluorescence spectra of the N-MQDs

Table 2 Detection of $As^{3+}$ in different real water samples using N-MQDs

| Real Sample | Analyte | Analyte concentration (mM) | Found concentration (mM) | Recovery (%) | RSD (%, $n = 6$) |
|---|---|---|---|---|---|
| Tap water | $As^{3+}$ | 0.088 | 0.09 | 102 | 2.2 |
| River water | $As^{3+}$ | 0.088 | 0.09 | 102.3 | 1.7 |
| Sea water | $As^{3+}$ | 0.088 | 0.087 | 98.8 | 2.0 |

were measured. As displayed in Table 2, very good recovery was observed in the range of 98–102% with good relative standard deviation. This indicates that the synthesized N-MQDs have tremendous potential to recognise $As^{3+}$ in real water samples, even in the presence of other contaminants.

## 4. Conclusions

Bright yellow fluorescent N-MQDs were successfully synthesized *via* a one-pot hydrothermal method using layered $Ti_3C_2$ as the starting material. The synthesized N-MQDs exhibit a narrow size distribution and high fluorescence with a maximum quantum yield of 13.8%. These nanoprobes were employed to detect $As^{3+}$ and MBTZ *via* a fluorescence "on/off/on" phenomenon. The yellow fluorescence of N-MQDs underwent a dramatic maximum quenching of 93% with treatment with $As^{3+}$. Static quenching was proven to be responsible for the fluorescence quenching behaviour. Upon the introduction of MBTZ to the complex, the fluorescence of the N-MQDs was restored due to the strong affinity of MBTZ with $As^{3+}$. Solid sensors were fabricated to identify $As^{3+}$ in wastewater using Whatman filter paper and cigarette filters. The adsorbed N-MQDs on the solid sensor effectively recognized $As^{3+}$ in water without any leaching. Real sample analysis confirmed that the N-MQDs can recover $As^{3+}$ in an effective manner in spite of the presence of other contaminants. This work will offer a straightforward approach for potential applications in environmental monitoring.

## Author contributions

Santanu Bera: conceptualization, data curation, writing – review & editing, writing – original draft. Susanta Kumar Bhunia: conceptualization, supervision, project administration, funding acquisition, writing – review & editing.

## Data availability

All the data that support the findings of this study are included within the article and the ESI,† or are available from the corresponding author upon reasonable request.

## Conflicts of interest

There are no conflicts to declare.

## Acknowledgements

This work was financially supported by Vellore Institute of Technology (VIT), Vellore under the Faculty Seed Grant (RGEMS) (Sanction Order No.: SG20240047) and DST INSPIRE funding (DST/INSPIRE Faculty Award/2018/DST/INSPIRE/04/2018/002484). S. Bera acknowledges VIT University for providing fellowship. The authors acknowledge Umarfaruk S. Sayyad and Dr. Somen Mondal for lifetime measurements.

## References

1 S. Dutta, S. Fajal and S. K. Ghosh, *Acc. Chem. Res.*, 2024, **57**, 2546–2560.
2 V. Singh, G. Ahmed, S. Vedika, P. Kumar, S. K. Chaturvedi, S. N. Rai, E. Vamanu and A. Kumar, *Sci. Rep.*, 2024, **14**, 7595.
3 P. A. Kobielska, A. J. Howarth, O. K. Farha and S. Nayak, *Coord. Chem. Rev.*, 2018, **358**, 92–107.
4 P. Mondal, J. Satra, D. N. Srivastava, G. R. Bhadu and B. Adhikary, *Inorg. Chem.*, 2023, **62**, 8874–8885.
5 P. Veerakumar, V. Veeramani, S.-M. Chen, R. Madhu and S.-B. Liu, *ACS Appl. Mater. Interfaces*, 2016, **8**, 1319–1326.
6 H. Lu, S. Xu and J. Liu, *ACS Sens.*, 2019, **4**, 1917–1924.
7 L. Zeng, D. Zhou, J. Gong, C. Liu and J. Chen, *Anal. Chem.*, 2019, **91**, 1724–1727.
8 J. Shantha Kumar, A. Jana, J. Raman, H. M. Veera, A. R. Kini, J. Roy, S. K. Jana, T. Thomas and T. Pradeep, *Environ. Sci. Technol. Lett.*, 2024, **11**, 831–837.
9 P. Nath, N. Priyadarshni and N. Chanda, *ACS Appl. Nano Mater.*, 2017, **1**, 73–81.
10 K. H. B. Haroon, V. UshaVipinachandran, S. Bera, V. Sithaiyan and S. K. Bhunia, *Environ. Sci.: Water Res. Technol.*, 2024, **10**, 2148–2161.
11 N. Yogarajah and S. S. Tsai, *Environ. Sci.: Water Res. Technol.*, 2015, **1**, 426–447.
12 K. E. Nachman, G. L. Ginsberg, M. D. Miller, C. J. Murray, A. E. Nigra and C. B. Pendergrast, *Sci. Total Environ.*, 2017, **581**, 221–236.
13 D. D'Ippoliti, E. Santelli, M. De Sario, M. Scortichini, M. Davoli and P. Michelozzi, *PLoS One*, 2015, **10**, e0138182.
14 R. N. Ratnaike, *Postgrad. Med. J.*, 2003, **79**, 391–396.
15 T. Samanta and R. Shunmugam, *Mater. Adv.*, 2021, **2**, 64–95.
16 M. S. Reid, K. S. Hoy, J. R. Schofield, J. S. Uppal, Y. Lin, X. Lu, H. Peng and X. C. Le, *TrAC, Trends Anal. Chem.*, 2020, **123**, 115770.

17 X. Le, M. Ma and N. A. Wong, *Anal. Chem.*, 1996, **68**, 4501–4506.
18 T. Nakazato and H. Tao, *Anal. Chem.*, 2006, **78**, 1665–1672.
19 J. Yang, L. Chen, J. Qi, F. Luo, L. Li, H. Wu, F. Cao and J. Gu, *Food Chem.*, 2024, **430**, 137007.
20 S. Rajendran, V. UshaVipinachandran, K. H. B. Haroon, I. Ashokan and S. K. Bhunia, *Anal. Methods*, 2022, **14**, 4263–4291.
21 S. Ben-Zichri, S. Rajendran, S. K. Bhunia and R. Jelinek, *Bioconjugate Chem.*, 2022, **33**, 1663–1671.
22 G. Zhu, D. Liao, J. Li and Y. Yi, *Chem. Commun.*, 2024, **60**, 12229–12232.
23 Y. Yi, W. Zeng and G. Zhu, *Talanta*, 2021, **222**, 121703.
24 G. Zhu, D. Liao, N. Hu, J. Li, Y. He and Y. Yi, *Sens. Actuators, B*, 2024, **413**, 135847.
25 F. Brette, D. Kourati, M. Paris, L. Loupias, S. Célérier, T. Cabioc'h, M. Deschamps, F. Boucher and V. Mauchamp, *J. Am. Chem. Soc.*, 2023, **145**, 4003–4014.
26 M. Naguib, M. Kurtoglu, V. Presser, J. Lu, J. Niu, M. Heon, L. Hultman, Y. Gogotsi and M. W. Barsoum, *Adv. Mater.*, 2011, **23**, 4248–4253.
27 A. VahidMohammadi, J. Rosen and Y. Gogotsi, *Science*, 2021, **372**, eabf1581.
28 T. Wang, W. Xiong, X. Tian and X. Xu, *Microchem. J.*, 2023, **194**, 109370.
29 G. Zhu, J. Hou, J. Xu, J. Li, C. Wang and Y. Yi, *Anal. Chim. Acta*, 2024, **1329**, 343250.
30 R. Singh, S. Kumar, S. Bera and S. K. Bhunia, *ACS Appl. Nano Mater.*, 2023, **6**, 19526–19550.
31 K. Huang, Z. Li, J. Lin, G. Han and P. Huang, *Chem. Soc. Rev.*, 2018, **47**, 5109–5124.
32 Q. Wang, F. Zhu, H. Cheng, S. Komarneni and J. Ma, *Chemosphere*, 2023, **328**, 138546.
33 X. Jiang, H. Wang, Y. Shen, N. Hu and W. Shi, *Sens. Actuators, B*, 2022, **350**, 130891.
34 A. Rafieerad, A. Amiri, G. L. Sequiera, W. Yan, Y. Chen, A. A. Polycarpou and S. Dhingra, *Adv. Funct. Mater.*, 2021, **31**, 2100015.
35 N. Liu, Q. Li, H. Wan, L. Chang, H. Wang, J. Fang, T. Ding, Q. Wen, L. Zhou and X. Xiao, *Nat. Commun.*, 2022, **13**, 5551.
36 Z. Xiao, Z. Li, X. Meng and R. Wang, *J. Mater. Chem. A*, 2019, **7**, 22730–22743.
37 M. Wan, J. Zhou, H. Yang, X. Dai, Y. Zheng, Z. Xia and L. Wang, *ACS Appl. Nano Mater.*, 2022, **5**, 11715–11722.
38 X. Wang, X. Zhang, H. Cao and Y. Huang, *Microchem. J.*, 2022, **180**, 107629.
39 F. Yan, J. Sun, Y. Zang, Z. Sun, H. Zhang, J. Xu and X. Wang, *Dyes Pigm.*, 2021, **195**, 109720.
40 F. Ai, C. Fu, G. Cheng, H. Zhang, Y. Feng, X. Yan and X. Zheng, *ACS Appl. Nano Mater.*, 2021, **4**, 8192–8199.
41 M. Liu, X. Pan, Y. Gan, M. Gao, X. Li, Z. Liu, X. Ma, M. Geng, X. Meng, N. Ma and J. Li, *Langmuir*, 2023, **39**, 13325–13334.
42 K. Jiang, S. Sun, L. Zhang, Y. Wang, C. Cai and H. Lin, *ACS Appl. Mater. Interfaces*, 2015, **7**, 23231–23238.
43 I. Ashokan and S. K. Bhunia, *J. Photochem. Photobiol., A*, 2023, **437**, 114489.
44 W. Luo, H. Liu, X. Liu, L. Liu and W. Zhao, *Colloids Surf., B*, 2021, **201**, 111631.
45 Y. Bai, Y. He, M. Wang and G. Song, *Sens. Actuators, B*, 2022, **357**, 131410.
46 C. Lin, C. Qiu, Y. Wang, Y. Liu, M. Rong and L. Niu, *Sens. Diagn.*, 2024, **3**, 431–439.
47 S. Rajendran, S. B. Zichri, V. UshaVipinachandran, R. Jelinek and S. K. Bhunia, *ChemNanoMat*, 2021, **7**, 545–552.
48 J. Gu, X. Lu, G. Li, B. Shan, J. Liu, Y. Qu, H. Ye, K. Xi and H. Wu, *Chem. Eng. J.*, 2023, **467**, 143445.
49 Z. Hallaji, Z. Bagheri and B. Ranjbar, *ACS Appl. Nano Mater.*, 2023, **6**, 3202–3210.
50 A. C. Khot, T. D. Dongale, J. H. Park, A. V. Kesavan and T. G. Kim, *ACS Appl. Mater. Interfaces*, 2021, **13**, 5216–5227.
51 X. He, Y. Li, C. Yang, L. Lu, Y. Nie and X. Tian, *Anal. Methods*, 2020, **12**, 5572–5580.
52 S. Roy, G. Palui and A. Banerjee, *Nanoscale*, 2012, **4**, 2734–2740.
53 S. Rajendran, D. V. Ramanaiah, S. Kundu and S. K. Bhunia, *ACS Appl. Nano Mater.*, 2021, **4**, 10931–10942.
54 X. Wang, Y. Lv and X. Hou, *Talanta*, 2011, **84**, 382–386.
55 S. Rajendran and S. K. Bhunia, *Colloids Surf., A*, 2023, **661**, 130882.
56 K. Radhakrishnan and P. Panneerselvam, *RSC Adv.*, 2018, **8**, 30455–30467.
57 R. Bandi, N. P. Devulapalli, R. Dadigala, B. R. Gangapuram and V. Guttena, *ACS Omega*, 2018, **3**, 13454–13466.
58 M. L. Desai, S. Jha, H. Basu, R. K. Singhal, T.-J. Park and S. K. Kailasa, *ACS Omega*, 2019, **4**, 19332–19340.
59 I. Ashokan and S. K. Bhunia, *Inorg. Chim. Acta*, 2024, **573**, 122312.
60 S. M. Basheer, P. Rasin, V. Manakkadan, V. N. V. Palakkeezhillam and A. Sreekanth, in *Schiff Base in Organic, Inorganic and Physical Chemistry*, IntechOpen, 2022.
61 T. V. Shishkanova, T. Tobrman, J. Otta, G. Broncová, P. Fitl and M. Vrňata, *J. Mater. Sci.*, 2022, **57**, 17870–17882.
62 D. Arocikia Jency, R. Parimaladevi, G. Vasant Sathe and M. Umadevi, *J. Cluster Sci.*, 2018, **29**, 281–287.
63 K. R. Vanapalli, H. B. Sharma, S. Anand, V. P. Ranjan, H. Singh, B. K. Dubey and B. Mohanty, *J. Hazard. Mater.*, 2023, **453**, 131387.
64 H. Kurmus and A. Mohajerani, *Waste Manage.*, 2020, **104**, 104–118.